

In the format provided by the authors and unedited.

Cation and anion immobilization through chemical bonding enhancement with fluorides for stable halide perovskite solar cells

Nengxu Li^{1,11}, Shuxia Tao ^{2,11}, Yihua Chen¹, Xiuxiu Niu³, Chidozie K. Onwudinanti⁴, Chen Hu⁵, Zhiwen Qiu¹, Ziqi Xu¹, Guan haojie Zheng¹, Ligang Wang¹, Yu Zhang¹, Liang Li¹, Huifen Liu¹, Yingzhuo Lun⁶, Jiawang Hong ⁶, Xueyun Wang ⁶, Yuquan Liu⁷, Haipeng Xie⁷, Yongli Gao^{7,8}, Yang Bai³, Shihe Yang^{5,9}, Geert Brocks^{2,10}, Qi Chen ³ and Huanping Zhou ^{1*}

¹Beijing Key Laboratory for Theory and Technology of Advanced Battery Materials, Key Laboratory of Polymer Chemistry and Physics of Ministry of Education, Department of Materials Science and Engineering, College of Engineering, Peking University, Beijing, China. ²Center for Computational Energy Research, Applied Physics, Eindhoven University of Technology, Eindhoven, the Netherlands. ³Experimental Center for Advanced Materials, School of Materials Science and Engineering, Beijing Institute of Technology, Beijing, China. ⁴Center for Computational Energy Research, DIFFER—Dutch Institute for Fundamental Energy Research, Eindhoven, the Netherlands. ⁵Department of Chemistry, The Hong Kong University of Science and Technology, Hong Kong, China. ⁶School of Aerospace Engineering, Beijing Institute of Technology, Beijing, China. ⁷Hunan Key Laboratory for Super-Microstructure and Ultrafast Process, College of Physics and Electronics, Central South University, Changsha, China. ⁸Department of Physics and Astronomy, University of Rochester, Rochester, NY, USA. ⁹Guangdong Key Lab of Nano-Micro Material Research, School of Chemical Biology and Biotechnology, Shenzhen Graduate School, Peking University, Shenzhen, China. ¹⁰Computational Materials Science, Faculty of Science and Technology and MESA+ Institute for Nanotechnology, University of Twente, Enschede, the Netherlands. ¹¹These authors contributed equally: Nengxu Li, Shuxia Tao. *e-mail: happy_zhou@pku.edu.cn

Supplementary Information

Cation and anion immobilization through chemical bonding enhancement with fluorides for stable halide perovskite solar cells

Nengxu Li^{1,11}, *Shuxia Tao*^{2,11}, *Yihua Chen*¹, *Xiuxiu Niu*³, *Chidozie K. Onwudinanti*⁴, *Chen Hu*⁵, *Zhiwen Qiu*¹, *Ziqi Xu*¹, *Guanhaojie Zheng*¹, *Ligang Wang*¹, *Yu Zhang*¹, *Liang Li*¹, *Huifen Liu*¹, *Yingzhuo Lun*⁶, *Jiawang Hong*⁶, *Xueyun Wang*⁶, *Yuquan Liu*⁷, *Haipeng Xie*⁷, *Yongli Gao*^{7,8}, *Yang Bai*³, *Shihe Yang*^{9,5}, *Geert Brocks*^{2,10}, *Qi Chen*³, *Huanping Zhou*^{*1}

¹ Beijing Key Laboratory for Theory and Technology of Advanced Battery Materials, Key Laboratory of Polymer Chemistry and Physics of Ministry of Education, Department of Materials Science and Engineering, College of Engineering, Peking University, Beijing 100871, P. R. China.

² Center for Computational Energy Research, Applied Physics, Eindhoven University of Technology, 5600MB, Eindhoven, the Netherlands.

³ Experimental Center for Advanced Materials, School of Materials Science and Engineering, Beijing Institute of Technology, Beijing 100081, P. R. China.

⁴ Center for Computational Energy Research, DIFFER – Dutch Institute for Fundamental Energy Research, De Zaale 20, 5612 AJ Eindhoven, The Netherlands.

⁵ Department of Chemistry, The Hong Kong University of Science and Technology, Clear Water Bay, Kowloon, Hong Kong, China.

⁶ School of Aerospace Engineering, Beijing Institute of Technology, Beijing 100081, P. R. China.

⁷ Hunan Key Laboratory for Super-microstructure and Ultrafast Process, Collage of Physics and Electronics, Central South University, Changsha, Hunan 410012, P.R. China.

⁸ Department of Physics and Astronomy, University of Rochester, Rochester 14627, USA.

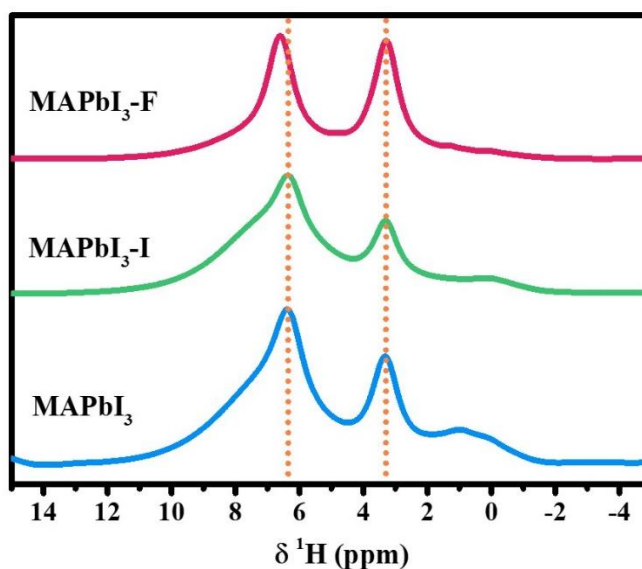
⁹ Guangdong Key Lab of Nano-Micro Material Research, School of Chemical Biology and Biotechnology, Shenzhen Graduate School, Peking University, Xili University Town, Shenzhen 518055, Guangdong, China.

¹⁰ Computational Materials Science, Faculty of Science and Technology and MESA⁺ Institute for Nanotechnology, University of Twente, 7500 AE Enschede, the Netherlands.

¹¹ These authors contributed equally to this work: Nengxu Li, Shuxia Tao.

Supplementary Note 1: Solid-state ^1H NMR results

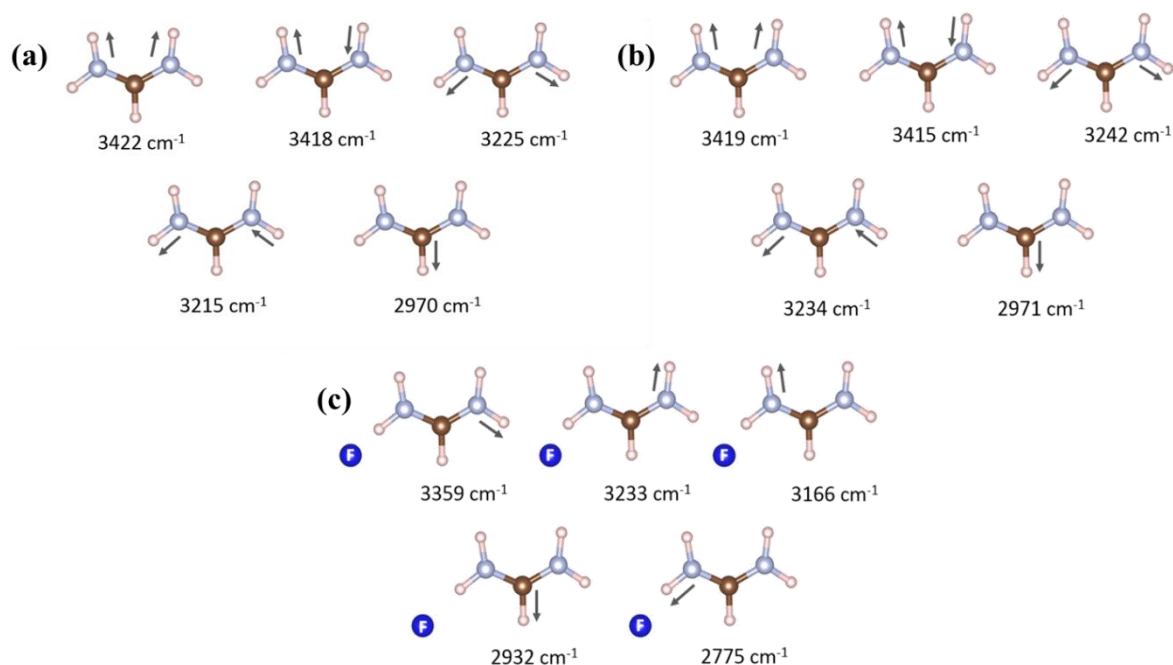
Clean perovskite (MAPbI_3) samples, NaI-containing ($\text{MAPbI}_3\text{-I}$) and NaF-containing ($\text{MAPbI}_3\text{-F}$) perovskite samples are characterized by solid-state ^1H NMR measurements. The spectra (**Supplementary Figure 1**) show two signals, which correspond to protons of NH_3 (left peak) and CH_3 (right peak)¹, respectively. It can be observed that the chemical shift of the NH_3 protons in $\text{MAPbI}_3\text{-F}$ (δ : 6.606) is larger than that in MAPbI_3 (δ : 6.376), and in $\text{MAPbI}_3\text{-I}$ (δ : 6.378). The formation of a hydrogen bond weakens the shielding of protons and results in shifting the resonance to a lower magnetic field, corresponding to higher δ -value. In addition, because the protons of NH_3 are easily split up, the corresponding peak signal has larger half width (both reference and NaI-containing perovskite). It is noteworthy that $\text{MAPbI}_3\text{-F}$ shows a sharper NH_3 peak, which indicates that these protons are more immobile than in the MAPbI_3 and $\text{MAPbI}_3\text{-I}$ samples. This can also be explained by the formation of hydrogen bonds in $\text{MAPbI}_3\text{-F}$. The ^1H NMR measurements support the Micro-FTIR results discussed in the main manuscript.



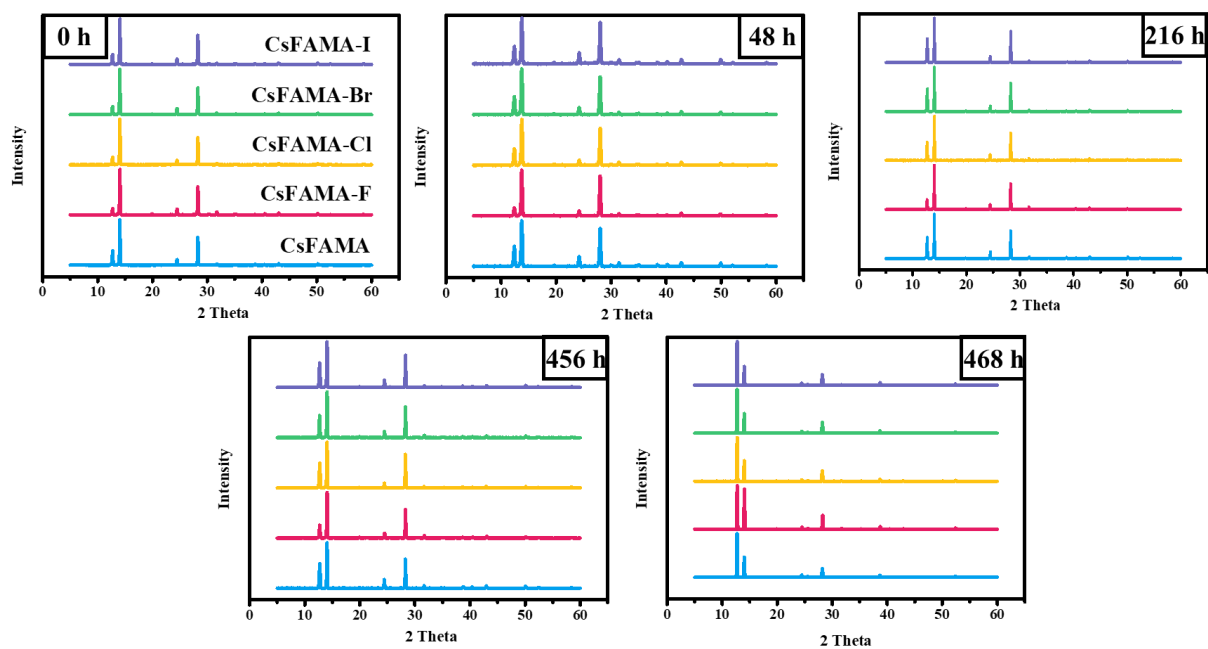
Supplementary Figure 1 Solid state ^1H NMR spectrum of reference perovskite (MAPbI_3), NaI-containing perovskite ($\text{MAPbI}_3\text{-I}$), and NaF-containing perovskite ($\text{MAPbI}_3\text{-F}$) samples.

Supplementary Note 2: Vibration modes of FA cation from DFT calculations

Diagonalizing the dynamical matrix, constructed by means of DFT calculations, we obtain the vibrational modes of the FA cations in FAPbI₃. These calculations are performed on a slab of FAPbI₃, where either a NaI unit, or a NaF unit is added at a FAI-terminated surface. The structures are shown in **Fig. 3a-b**. Using selective dynamics, we calculate the vibrational modes of the organic cations. In **Supplementary Figure 2** the hydrogen stretch modes are depicted of FA ions at the clean FAI-terminated surface of FAPbI₃, and of FA ions near NaI or NaF. Adding NaI hardly changes the frequencies of these modes, whereas adding NaF leads to substantial shifts. In the clean system and in the NaI system, the five hydrogen stretch modes can be divided into two N-H doublets with frequencies $\sim 3420\text{ cm}^{-1}$ and $\sim 3220\text{ cm}^{-1}$, respectively, and a single C-H mode at $\sim 2970\text{ cm}^{-1}$. This pattern is dictated by the symmetry of the FA ion, where the coupling between vibrations of hydrogen atoms bonded to different atoms is small. This symmetry is clearly broken in the NaF system, and the two N-H doublets are split up. Note that the frequency of the hydrogen atom closest to an F ion is shifted to a much lower frequency (2775 cm^{-1}), which is a clear sign of the formation of a hydrogen bond.



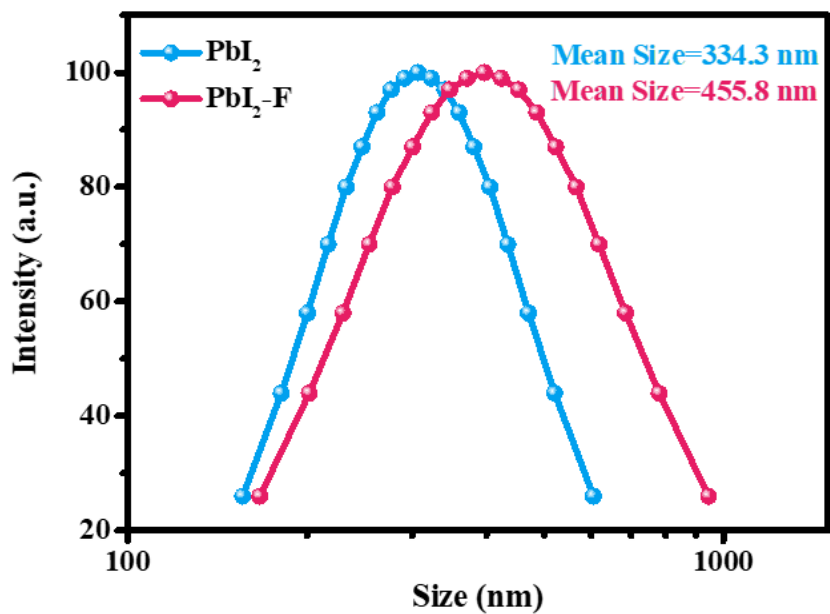
Supplementary Figure 2 The N-H and C-H stretching modes. (a) a FA molecule at the FAI terminated FAPbI₃, and of FA ions near (b) NaI or (c) NaF.



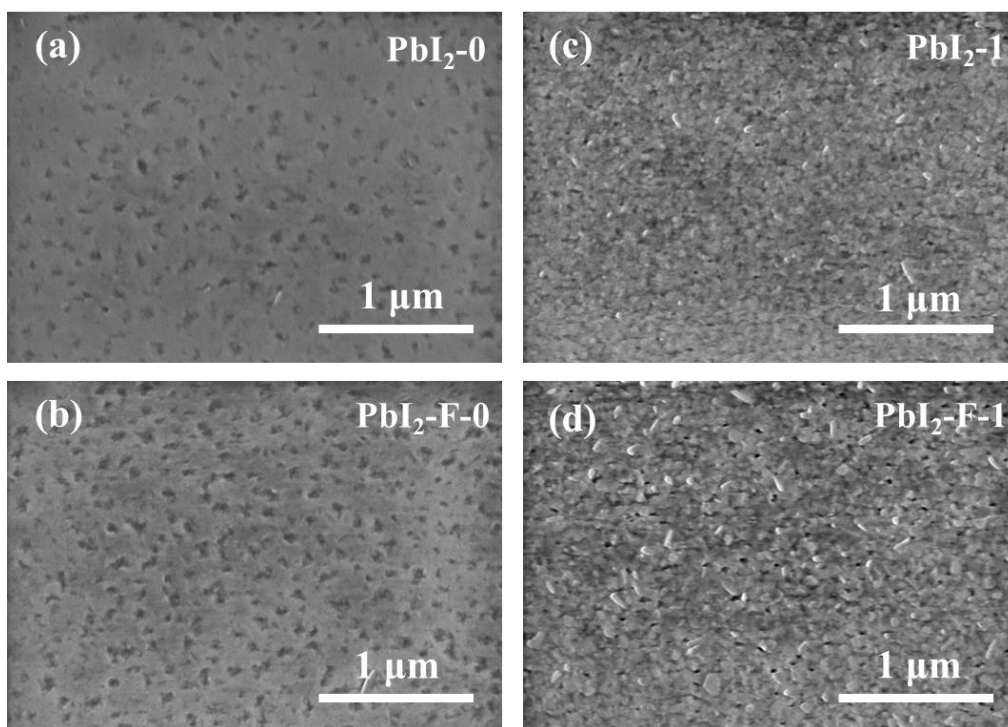
Supplementary Figure 3 XRD patterns of reference (CsFAMA) and NaX-containing perovskite films (CsFAMA-X) after annealing at 85°C in nitrogen for 0 h, 48 h, 216 h, 456 h, and subsequent annealing at 100 °C in air for 12 h (added up to 468 h).

Supplementary Note 3: SEM results and analyses

SEM images of perovskite thin films without and with NaX additives are shown in **Fig. 1f**. All these films are pinhole-free. However, using the same fabrication parameters, the grain sizes in the CsFAMA-F and CsFAMA-Cl films are larger than those in the CsFAMA film, while grain sizes in CsFAMA-Br and CsFAMA-I films are almost as in CsFAMA. The increased grain size of the Cl-containing material has also been reported in a recent study². However, this is the first time where it is shown that CsFAMA-F sample also has a larger grain size. To understand this, we conduct dynamic light scattering (DLS) measurements on the PbI₂ solutions with and without NaF, using the latter as a reference. As seen in **Supplementary Figure 4**, the mean diameter of PbI₂-dimethyl sulfoxide (DMSO) complexes in the reference is measured to be 334.3 nm, while in the case NaF is added, the PbI₂-DMSO complex diameter increases to 455.8 nm. We speculate that the stronger interaction between PbI₂ and F leads to larger colloidal particles. Interestingly, the morphology of PbI₂ films (**Supplementary Figure 5**) is also modified by NaF. Larger PbI₂ crystals are formed if NaF is added, and the PbI₂ film has a larger number of voids per unit volume, regardless of the annealing process. We attribute the increased void density to the inhomogeneity of the PbI₂ precursor solution, caused by larger PbI₂ colloidal particle sizes with the introduction of NaF. Such a “porous PbI₂” film with larger grain size obtained by NaF addition may possess fewer nucleation sites, resulting in a reduced nucleation rate during perovskite formation. Hence the slower nucleation rate in a PbI₂ film in the presence of NaF, results in a larger grain size in the perovskite film, if the growth rate is fixed, consistent with other reports³.



Supplementary Figure 4 Size distributions of PbI₂-DMSO complexes in reference (PbI₂) and NaF-containing (PbI₂-F) precursor solutions detected by dynamic light scattering (DLS).



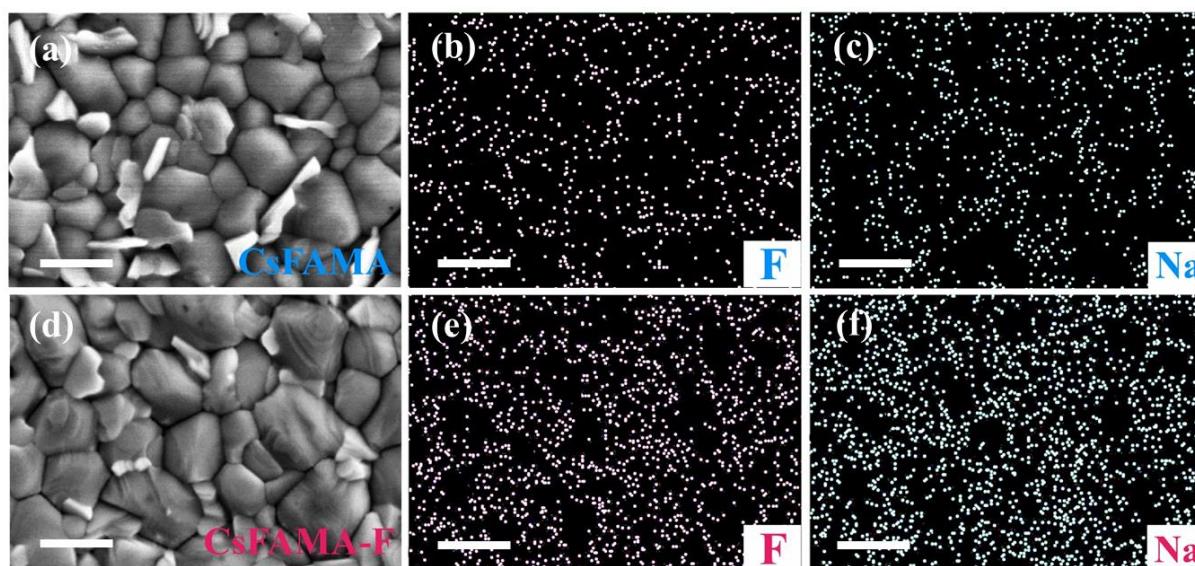
Supplementary Figure 5 Top view SEM images of PbI_2 thin films obtained by spin-coating. (a) Without NaF additive and without annealing ($\text{PbI}_2\text{-0}$). **(b)** With NaF additive and without annealing ($\text{PbI}_2\text{-F-0}$). **(c)** Without NaF additive and with annealing at 70 °C for 1 min ($\text{PbI}_2\text{-1}$). **(d)** With NaF additive and with annealing at 70 °C for 1 min ($\text{PbI}_2\text{-F-1}$).

Supplementary Table 1 TRPL results. The obtained carrier lifetimes of CsFAMA and CsFAMA-F perovskite films.

Sample	Lifetime τ_1 /ns	Lifetime τ_2 /ns
CsFAMA	30.82	193.29
CsFAMA-F	97.16	401.64
CsFAMA-Cl	39.60	287.86
CsFAMA-Br	49.68	234.62
CsFAMA-I	64.02	232.76

Supplementary Note 4: EDX results and analyses

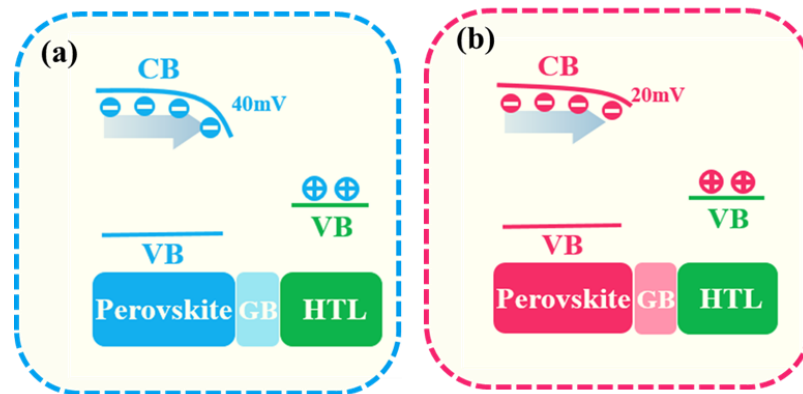
We collected the energy dispersive X-ray spectroscopy (EDS) signals of F and Na on both CsFAMA and CsFAMA-F samples, keeping the same fabrication and measurement conditions. It can be found that even on reference (CsFAMA) samples, we still find a certain amount of signals of NaF (**Supplementary Figure 6b-c**). Indeed, these signals are noise, and due to the much low orbital energy of F and Na atoms, the noise of the technique can be easily mistaken into the signals of NaF. In comparison, the signals of Na and F of CsFAMA-F sample (**Supplementary Figure 6e-f**) are stronger. In consideration of the same exposure time during EDX measurements on two samples, the signals on CsFAMA-F sample are not all noise. This indicates the existence of NaF species in CsFAMA-F sample, confirming successful incorporation of NaF species into the perovskite films.



Supplementary Figure 6 Energy dispersive X-ray spectroscopy (EDS) signals of F and Na on both CsFAMA and CsFAMA-F samples. The top-view field emission scanning electron microscopy (FE-SEM) images (**a**, **d**) and corresponding energy dispersive X-ray spectroscopy (EDX) mapping of CsFAMA (**b**, **c**) and CsFAMA-F (**e**, **f**) perovskite thin films. The scale bar is 1 μm .

Supplementary Note 5: SKPM results and analyses

From the SKPM results (**Fig. 2c-d**) of CsFAMA and CsFAMA-F samples, we observe that the CsFAMA perovskite film exhibits a higher surface potential at GBs than in the grain centers of about 40 mV. The corresponding value for CsFAMA-F perovskite films is only about 20 mV. Therefore, we speculate that a small amount of NaF may be beneficial for decreasing the charge accumulation at GBs, leading to lower GB potential in CsFAMA-F perovskite. Furthermore, as the surface potential at GBs is higher than in the grain bulks, passivated GBs may reduce the probability of electron flow from the grain bulk to grain boundaries, and may also facilitate hole extraction by decreasing the barriers at the GBs. As illustrated in the scheme shown in **Supplementary Figure 7**, the CsFAMA perovskite has a deeper downward band bending around GBs. Therefore, the electrons are attracted while the holes are repelled. The potential profile follows a similar pattern found in Cu(In,Ga)Se₂ films⁴. However, in contrast to the latter, in PSCs the hole transport layer fabricated by spin-coating can easily infiltrate into the GBs of perovskite films to extract holes. In this regard, a deep downward band bending around GBs hinders the hole extraction and increases charge recombination at these interfaces. Adding NaF, the difference between the GBs and grain center potentials is greatly diminished, suppressing the barrier for hole extraction and reducing the probability of electron injection into GBs.



Supplementary Figure 7 The scheme of band bending at GBs. **(a)** CsFAMA and **(b)** CsFAMA-F perovskites.

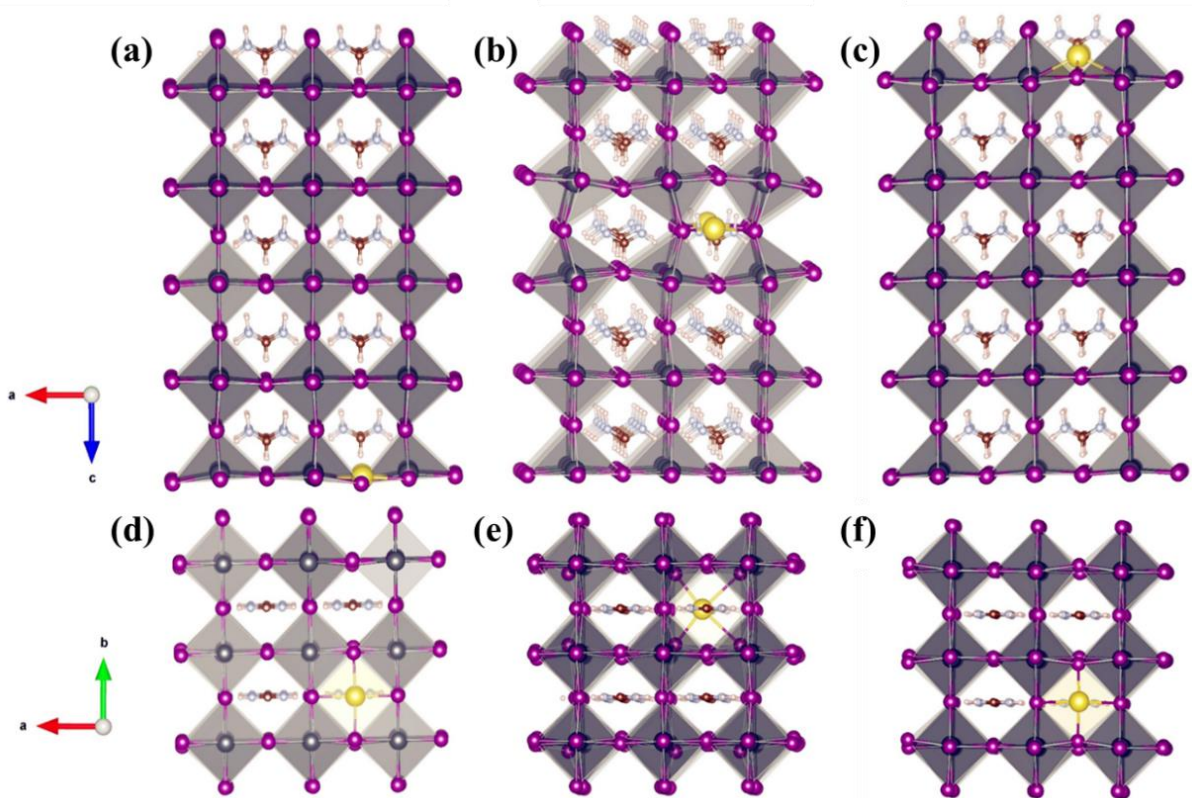
Supplementary Note 6: Computational models and optimized structure

To investigate the energetics of incorporation of Na or F ions into a perovskite lattice, we have constructed slab models of FAPbI₃. The slabs consist of 5 perovskite layers in the z direction, and have a FAI-terminated surface on one side, and a PbI₂-terminated surface on the other side. The in-plane structure is modelled using a 2x2 cell in the x and y directions.

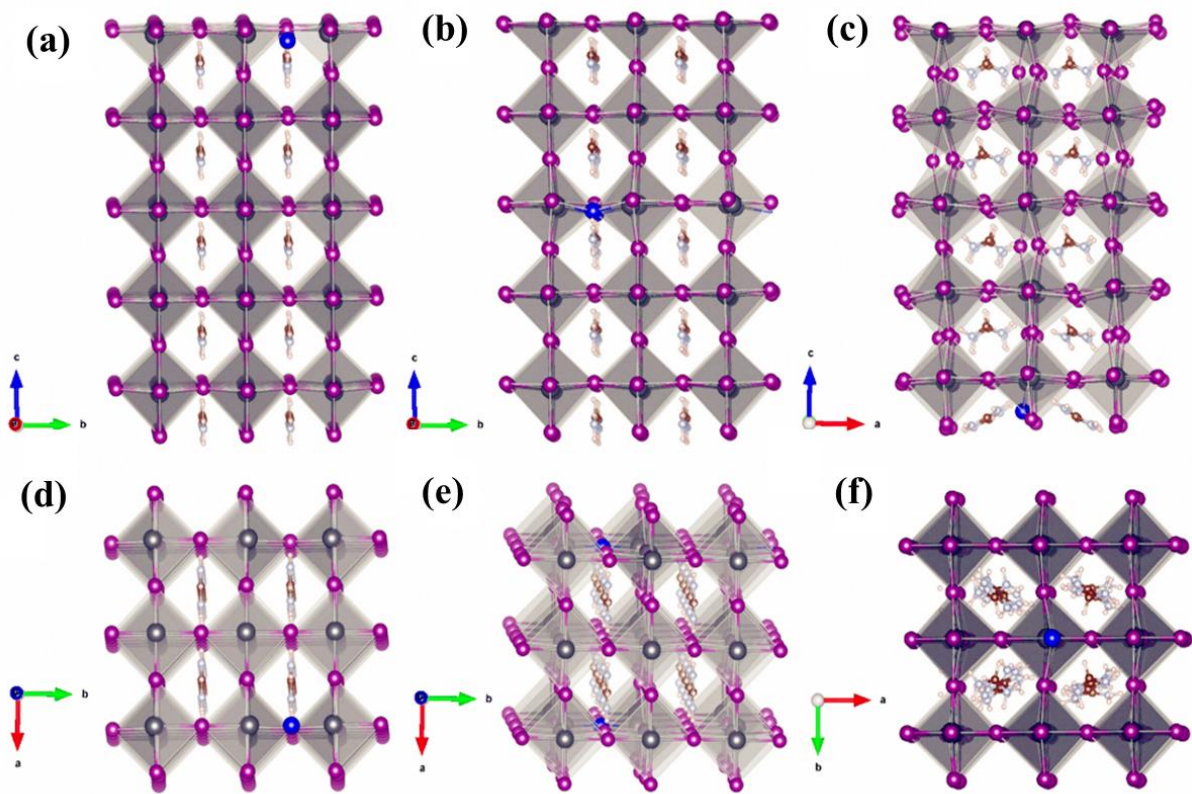
Supplementary Figure 8 shows the optimized structures of slabs in which one of the FA cations is substituted by a Na cation at **(a)** the PbI₂-terminated surface, **(b)** in the middle of the slab, and **(c)** at the FAI-terminated surface. The latter gives the lowest energy. Using this as reference, **(a)** has an energy of 0.06 eV, and **(b)** has an energy of 0.30 eV. The energies indicate that it is more favorable to incorporate a Na ion at a surface or grain boundary, instead of in the bulk. In the optimized surface structures, the Na ion has actually moved to an interstitial site (rather than a lattice A site), see **Supplementary Figure 8d and 8f**.

Supplementary Figure 9 shows the optimized structures of slabs in which one of the I anions is substituted by a F anion at **(a)** the PbI₂-terminated surface, **(b)** in the middle of the slab, and **(c)** at the FAI-terminated surface. The latter gives the lowest energy. Using this as reference, **(a)** has an energy of 3.50 eV, and **(b)** has an energy of 3.57 eV. The energies show that incorporation of F at a FAI-terminated surface is far more favorable than at a PbI₂-terminated surface, or in the bulk. Incorporated in the FAI-terminated surface, the F ion relaxes inwards, contracting the lattice around it. As discussed in the main text, and in **Supplementary Figure 2**, the FA ions surrounding the F site reorient toward the F ion, where the closest FAs form hydrogen bonds with F.

The above analysis confirms the Na and F are most likely incorporated on the surfaces of perovskite films. The underlying reason is likely that the Na and F ions are too small to be incorporated in the bulk of perovskite. The surfaces allow for a better relaxation of strains induced by the size mismatch between the small cation or anion, Na or F, and the larger cations or anions in the perovskites, FA/MA or I/Br.



Supplementary Figure 8 DFT optimized structures for evaluating the location of Na ions. In all structures, one Na ion (yellow spheres) substitutes one FA cation. (a) (b) (c) are side views and (d) (e) (f) are top views of incorporation of Na at PbI_2 terminated surface, bulk and FAI terminated surfaces.



Supplementary Figure 9 DFT optimized structures for evaluating the location of F ions. In all structures, one F ion (blue spheres) substitutes one I anion. (a) (b) (c) are side views and (d) (e) (f) are top views of incorporation of F at PbI_2 terminated surface, bulk and FAI terminated surfaces. This sets of structural optimization was calculated using force convergence criterion of $40 \text{ meV}/\text{\AA}$.

Supplementary Note 7: Chemical bonding analyses

In addition to the energy calculations, we have carried out an in-depth analysis of the chemical bonding for a thorough understanding of the bonding in the perovskites. The bonds of main interest are those between I-Pb, Na-I, Na-F and F-Pb on the FAI- and PbI₂-terminated surfaces. We investigate the strength of the chemical bonding by analyzing both the ionic and covalent contributions to a bond. The ionic contribution to a bond can be characterized by a net atomic charge, which quantifies the electron transfer between atoms⁵⁻⁶. The covalent contribution can be identified by the bond order, which correlates with the electron density at a bond-critical point (a saddle-point of the electron density along the bond path)⁵⁻⁶. The higher the bond order, the stronger a covalent bond.

Our chemical bonding analysis allows us to identify the change in bonding strength induced by the incorporation of Na and F. As discussed in the main text (**Fig. 3c**) we observe that (i) Na ions slightly increase the ionic bonding with the surrounding I ions and (ii) F ions significantly increase the ionic bonding with Pb.

Supplementary Note 8: Formation energy of FA⁺ vacancy on perovskite surfaces

Supplementary Figure 10 shows the optimized structure of a cation (Na) and an anion (F) incorporated on the FAI-terminated surface. We replace one FA⁺ cation with Na⁺ and one I with F⁻. We calculate the formation energies of FA cation vacancies at the surface of this structure. As references, we also calculate the same formation energy for a surface where F is replaced by I, and for an unmodified FAI-terminated surface. The details of the computational procedure are as follows.

The FA⁺ defect formation energy is defined as:

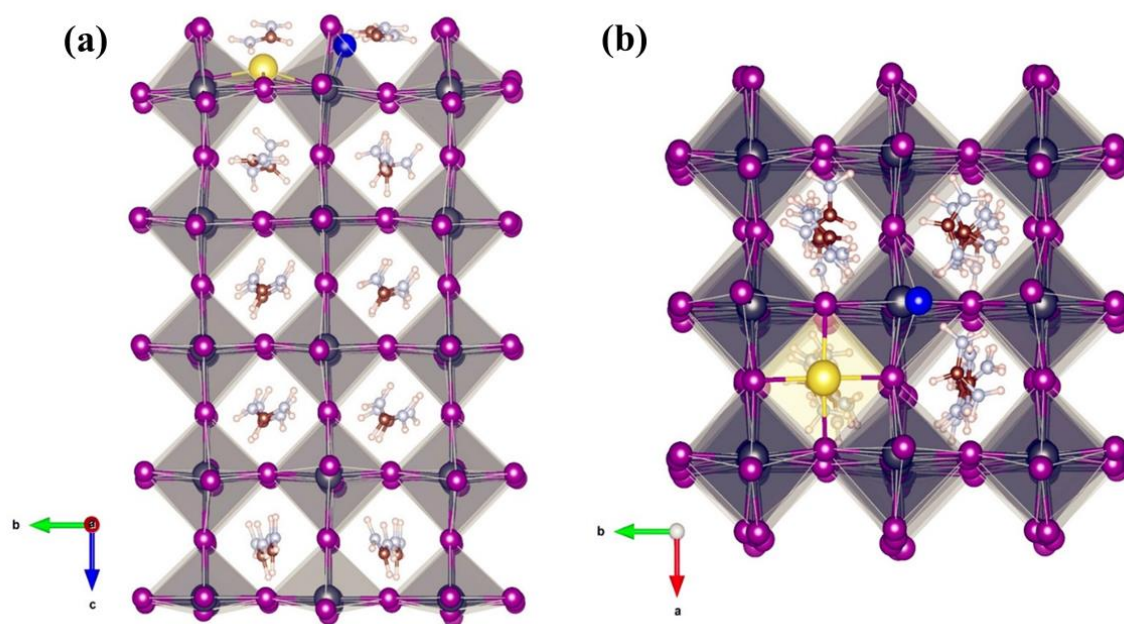
$$\Delta E_{\text{FAvac}} [\text{FA}^+] = E_{\text{tot}} [\text{FA}^+\text{vac}] - E_{\text{tot}} [\text{surface}] + \mu[\text{FA}] + E_{\text{Fermi}},$$

Where $E_{\text{Tot}} [\text{FA}^+\text{vac}]$ and $E_{\text{tot}} [\text{surface}]$ are the total energies of the surfaces with and without FA⁺ vacancy, respectively, and E_{Fermi} and $\mu[\text{FA}]$ are the Fermi energy, and the chemical potential of FA, respectively. The latter two are assumed to be the same for all three perovskites. This approximation is valid since the important parameters during synthesis of these perovskites, such as precursor concentration, the source of FA⁺, temperature and deposition procedure, are kept the same in our experiments. In addition, experimentally the Fermi energy levels in the three perovskites only vary by about 0.1 eV (**Supplementary Figure 17**).

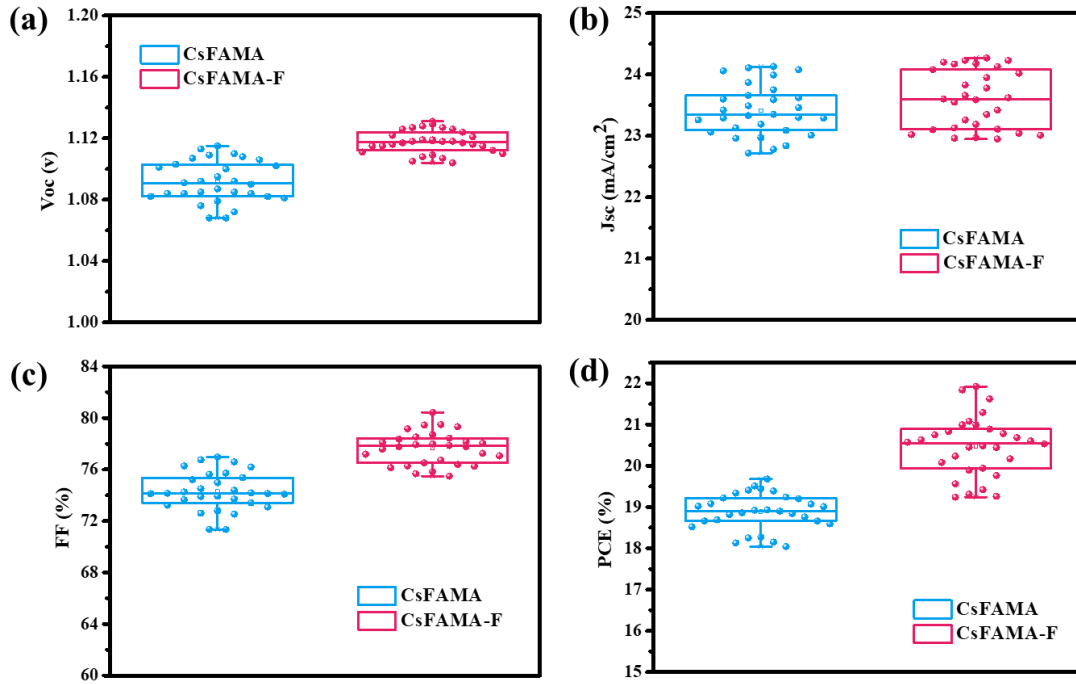
Inspired by Saidaminov et al⁷, we define the suppression of FA vacancy formation due to the introduction of Na⁺ and F⁻, or Na⁺ and I⁻, as:

$$\Delta\Delta E_{\text{FAvac}} = \Delta E_{\text{FAvac}} [\text{FA}^+] [\text{NaI/NaF}] - \Delta E_{\text{FAvac}} [\text{FA}^+][\text{ref}],$$

Where $\Delta E_{\text{FAvac}} [\text{FA}^+] [\text{NaI/NaF}]$ is the formation energy of a FA⁺ defect in the presence of Na-I or Na-F, respectively, and $\Delta E_{\text{FAvac}} [\text{FA}^+] [\text{ref}]$ the one of the unmodified FAI-terminated surface. $\Delta\Delta E_{\text{FAvac}}$ turns out to be positive in the presence of Na-I or Na-F, indicating that the formation of FA⁺ vacancies is suppressed. **Fig. 3d** shows that this formation energy increases significantly by 0.55 eV in the presence of Na-F, while in the presence of Na-I the increase is only a moderate 0.12 eV.



Supplementary Figure 10 (a) Side view and (b) top view of the location of Na and F on the FAI terminated surface of FAPbI_3 perovskites from DFT calculations.



Supplementary Figure 11 The performance of 60 devices without (CsFAMA) and with (CsFAMA-F) NaF additive; (a) open circuit voltage, (b) short-circuit current, (c) fill factor, (d) power conversion efficiency.

Supplementary Table 2 Detailed parameters for 60 devices without (CsFAMA) and with (CsFAMA-F) NaF additive.

Sample	V_{oc} (V)	J_{sc} (mA/cm^2)	FF (%)	PCE (%)
CsFAMA	1.086 ± 0.028	23.42 ± 0.71	74.17 ± 2.80	18.86 ± 0.82
CsFAMA-F	1.118 ± 0.015	23.61 ± 0.66	77.89 ± 2.47	20.56 ± 1.36

证书编号 GXtc2018-0672
Certificate No.

中国计量科学研究院是国家最高的计量科学研究中心和国家法定计量技术机构。1999年授权签署了国际计量委员会(CIPM)(国家计量基(标)准和国家计量院签发的校准与测量证书互认协议(CIPM MRA)。The National Institute of Metrology (NIM) is China's national metrology institute (NMI) and a state-level legal metrology institute. NIM is China's signatory to the Mutual Recognition of National Measurement Standards and of Calibration and Measurement Certificates Issued by National Metrology Institutes (CIPM MRA) which is arranged by the International Committee of Weights and Measures (CIPM).

中国计量科学研究院的质量管理体系符合 ISO/IEC17025 标准, 通过中国合格评定国家认可委员会和亚太计量规划组织(APMP)联合评审的校准和测量能力(CMCs)在国际计量局(BIPM)关键比对数据库中公布。NIM's quality management system meets requirements of the ISO/IEC 17025. Its Calibration and Measurement Capabilities (CMCs) that are peer reviewed both by China National Accreditation Service for Conformity Assessment (CNAS) and the Asia Pacific Metrology Programme (APMP) are published in the International Bureau of Weights and Measures (BIPM) Key Comparison Database (KCDB).

2011年, 中国计量科学研究院和中国合格评定国家认可委员会就认可领域的技术评价活动签署了谅解备忘录, 承认中国计量科学研究院的计量支撑作用和出具的校准/检测结果的溯源效力。NIM and CNAS signed a Memorandum of Understanding (MOU) for Recognition of Technical Assessment in Laboratory Accreditation Field in 2011, in which CNAS recognizing the technical supporting role of NIM in laboratory accreditation and the traceability of NIM's calibration / test results.

测试结果的评估和表述均符合 JJF1059 系列标准的要求。The evaluation and expression of uncertainty of the test results are in line with the requirements of JJF1059 series standards.

测试所依据的技术文件(代号、名称) Reference documents (Code, Name)
Measurement of photovoltaic current-voltage characteristics (IEC60904-1)
太阳能电池校准规范: 光电性能 (JJF 1622-2017) (Calibration Specification of Solar Cells: Photoelectric Properties)

测试环境条件及地点 Test place and environment
温度 Temperature: 25.1 °C 地点 Location: 计量院和平里5号楼401
湿度 Humidity: 17.3 %RH 其它 Others:

测试使用的计量基(标)准装置(含标准物质)主要仪器
Reference Standards (Including the Reference Material) / Instruments used

名称 Name	测量范围 Measurement Range	不确定度/准确度等级 Uncertainty/Accuracy	证书编号 Certificate No.	证书有效期至 Due Date (YYYY-MM-DD)
太阳能电池光电性能校准装置 Measurement Standard	I_{sc} : (0.1-10) A V_{oc} : (0.1-200)V P_{max} : (0.01-500) W	I_{sc} : 1.5% (k=2) V_{oc} : 0.5% (k=2) P_{max} : 1.6% (k=2)	[2015]国量标计证字第286号	2019-07-05
标准太阳能电池 Reference solar cell	I_{sc} : (0-200) mA	1.2% (k=2)	GXtc2018-0439	2019-03-12

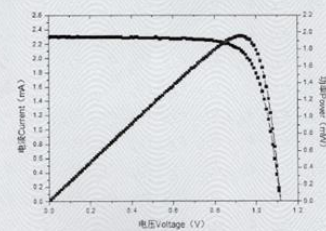
证书编号 GXtc2018-0672
Certificate No.

测试结果 Calibration Results

- 1. 测试条件 Test Conditions:**
标准太阳能电池: 单晶硅 (81#);
Reference Solar Cell: mono-Si (81#);
太阳模拟器: 双光源太阳模拟器, AAA 级;
Solar Simulator Classification: double-light source in AAA classification;
温度传感器/控制系统: 无;
Temperature Sensor/Control System: None;
Mask (Y/N): Y;
电压设置: -0.1V~1.2V; 间隔: 0.01V
Scan Parameter: From -0.1V to 1.2V with 0.01V interval
光阑 Mask (Y/N): Y
扫描时间: 39 秒 扫描点数: 131
Scan Time: 39 s Scan Point: 131

- 1-V 特性参数 I-V Characteristic parameters:**
以上述标准太阳能电池标定太阳模拟器辐照度至 1000 W/m², 校准被测太阳能电池的 I-V 特性曲线和参数如下:
By using the above reference solar cell to calibrate the solar simulator's irradiance to 1000 W/m², the I-V characteristic curve and parameters as follows:

扫描方向: 正扫
Scan Direction: forward



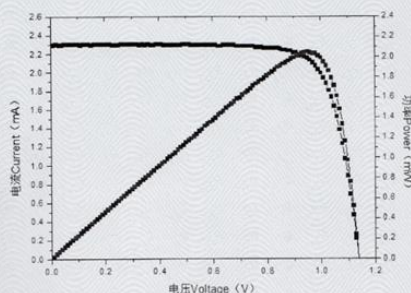
证书编号 GXtc2018-0672
Certificate No.

测试结果 Calibration Results

有效面积 (mm ²)	短路电流 I_{sc} (mA)	开路电压 V_{oc} (V)	最大功率 P_{max} (mW)
9.408	2.29	1.10	1.96

最大功率电流 I_{max} (mA)	最大功率电压 V_{max} (V)	填充因子 FF (%)	转换效率(PCE) η (%)
2.10	0.93	77.3	20.8

扫描方向: 反扫
Scan Direction: reverse



证书编号 GXtc2018-0672
Certificate No.

测试结果 Calibration Results

有效面积 (mm ²)	短路电流 I_{sc} (mA)	开路电压 V_{oc} (V)	最大功率 P_{max} (mW)
9.408	2.29	1.14	2.05

最大功率电流 I_{max} (mA)	最大功率电压 V_{max} (V)	填充因子 FF (%)	转换效率(PCE) η (%)
2.15	0.95	78.2	21.7

注 Note:

1. 测试所用 mask 的面积为 9.408mm² (证书编号: CDjc2018-0407)。
The mask area is 9.408mm² (Certificate No.: CDjc2018-0407).
2. 此数据仅对被测样品当时状态有效。
The data apply only at the time of the test for the sample.
(以下空白)

声明 Statement:

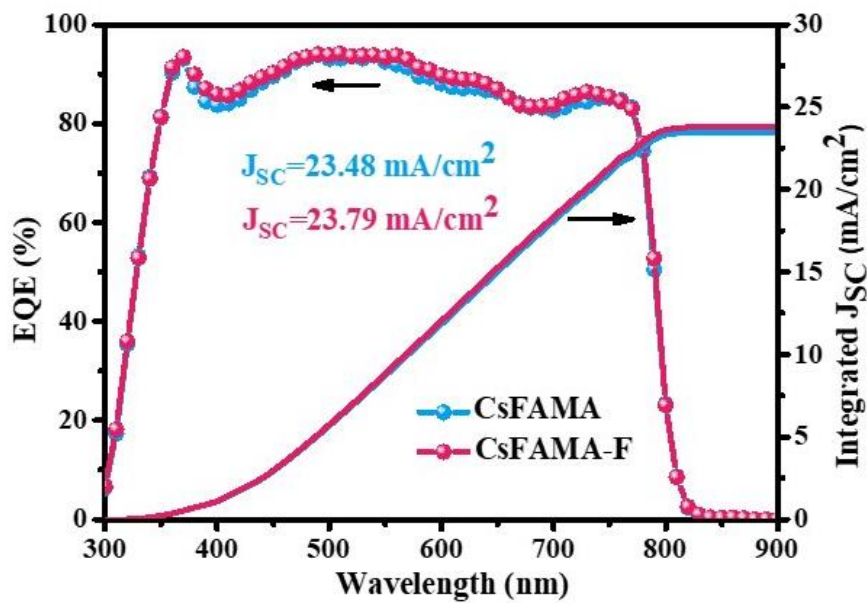
1. 我院仅对加盖“中国计量科学研究院校准专用章”的完整证书负责。
NIM is ONLY responsible for the complete certificate with the calibration stamp of NIM.
2. 本证书的测试结果仅对所校准的仪器有效。
The certificate is ONLY valid for the tested instrument.
3. 本证书用中英文两种语言表达, 准确含义以中文为准。
The certificate is reported in both English and Chinese, with the Chinese version as standard.

测试员:  核验员: 

Supplementary Figure 12 Certificated results by the National Institute of Metrology, China (NIM, China). The forward scan is performed from -0.1 V to 1.2 V at 33 mV/s, with a PCE of 20.8% (V_{oc} =1.10 V, I_{sc} =2.29 mA, FF=77.3%). The reverse scan is performed from 1.2 V to -0.1 V at 33 mV/s, with a PCE of 21.7% (V_{oc} =1.14 V, I_{sc} =2.29 mA, FF=78.2%). The device has an active area of 0.09408 cm².

Supplementary Note 9: EQE results and analyses

Supplementary Figure 13 shows the spectral response of the external quantum efficiency (EQE) of the devices, as well as the integrated current derived by calculating the overlap integral between EQE spectrum and standard AM1.5 solar emission. Although both types of devices exhibit the same shape of spectrogram, the CsFAMA-F cells have slightly higher EQE values and integrated current (23.48 mA/cm² and 23.79 mA/cm² for CsFAMA and CsFAMA-F PSCs, respectively). This result also agrees well with the value of short-circuit current density obtained from J-V results.



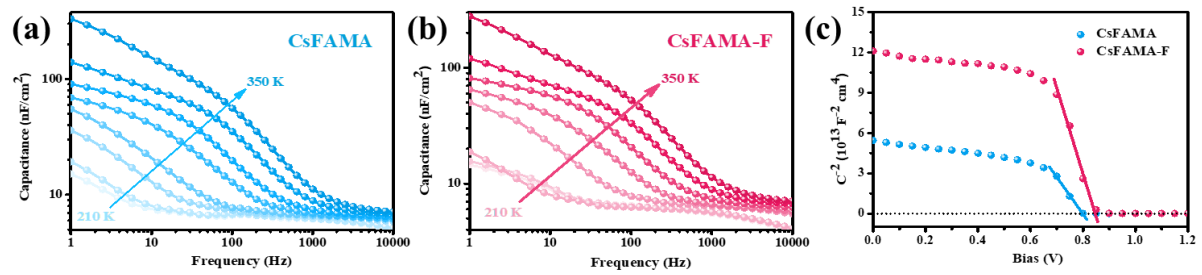
Supplementary Figure 13 External quantum efficiency spectrum together with integrated J_{SC} for the CsFAMA and CsFAMA-F PSCs.

Supplementary Note 10: AS and Mott–Schottky analyses

Admittance spectroscopy (AS) combined with Mott–Schottky analysis is a powerful technique to find out both the energy levels and the density distribution of trap states. This technique has been extensively applied to $\text{Cu}_2\text{ZnSnS}_4$ solar cells, organic solar cells, and PSCs⁸⁻¹⁰, where it has proven to be effective. As the previous literature reported¹¹, for a p-type perovskite semiconductor, the defect activation energy (E_a) can be calculated by the trap state energy level (E_T) and the perovskite VBM energy level (E_{VBM}) ($E_a = E_T - E_{\text{VBM}}$). E_a and the characteristic transition angular frequency (ω_0) can be formulated in the following equation: $\omega_0 = \beta T^2 \exp(-\frac{E_a}{k_B T})$, where β is a temperature dependent parameter, T is the temperature and k_B is the Boltzmann's constant. The derivative of the capacitance spectrum can be used to determine ω_0 . According to this relation, the value of E_a can be obtained from the slope of the graph by fitting the Arrhenius formula: $\ln(\frac{\omega_0}{T^2}) = \ln\beta - \frac{E_a}{k_B T}$, the distribution of trap state density can be derived from the equation¹¹: $N_T(E_\omega) = -\frac{V_{bi}}{qW} \frac{dC}{d\omega} \frac{\omega}{k_B T}$, $E_\omega = k_B T \ln(\frac{\beta T^2}{\omega})$, where V_{bi} is the built-in potential, W is the depletion width, q is the elementary charge, C is the capacitance, and ω is the applied angular frequency. The Mott-Schottky junction was obtained by capacitance-voltage measurement, which was analyzed to obtain V_{bi} and W . According to the depletion approximation¹², the C , V_{bi} , and W at the junction can be expressed in the relation: $\frac{C}{A} = \frac{\epsilon\epsilon_0}{W} = \sqrt{\frac{q\epsilon\epsilon_0 N}{2(V_{bi}-V)}}$, where A is the active area, ϵ is the static permittivity of perovskite, ϵ_0 is the permittivity of free space, N is the apparent doping profile in the depleted layer, and V is the applied bias. A Mott-Schottky plot: $\frac{A^2}{C^2} = \frac{2(V_{bi}-V)}{q\epsilon\epsilon_0 N}$ describes a straight line where the intersection on the bias axis determines V_{bi} and the slope gives the impurity doping density N . Then, the depletion width $W = \sqrt{\frac{2\epsilon\epsilon_0 V_{bi}}{qN}}$ corresponding to the zero bias can be calculated.

Supplementary Figure 14a-b display the temperature-dependent AS of the CsFAMA and CsFAMA-F devices measured at temperatures ranging from 210 to 350 K without illumination. Shown in **Fig. 4d**, the corresponding Arrhenius plots of these two devices describe the relationship between the characteristic transition frequencies and temperatures. The calculated defect activation energies (E_a) of the CsFAMA and CsFAMA-F samples are 0.275 and 0.201 eV, respectively. The built-in potential (V_{bi}) and the depletion width (W) are determined from

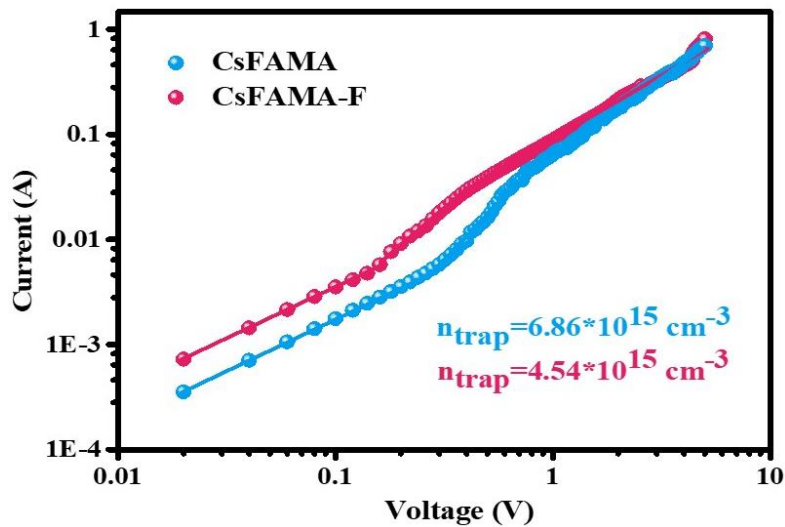
the Mott–Schottky analysis of the data measured at a frequency of 1 kHz with bias potential from 0 to 1.2 V. **Supplementary Figure 14c** indicates that the built-in potentials of the CsFAMA and CsFAMA-F samples are 0.80 and 0.90 V, and the corresponding depletion widths are 133 and 207 nm, respectively. The density distribution and energy levels of trap states in these two devices are presented in **Fig. 4e**.



Supplementary Figure 14 Admittance spectroscopy (AS) and Mott–Schottky analysis of perovskite solar cells. (a) Admittance spectra of CsFAMA cell. **(b)** Admittance spectra of CsFAMA-F cell. These are measured at gradient temperatures between 210 and 350 K with a step of 20 K. **(c)** Mott–Schottky analysis at 1 kHz.

Supplementary Note II: SCLC results and analyses

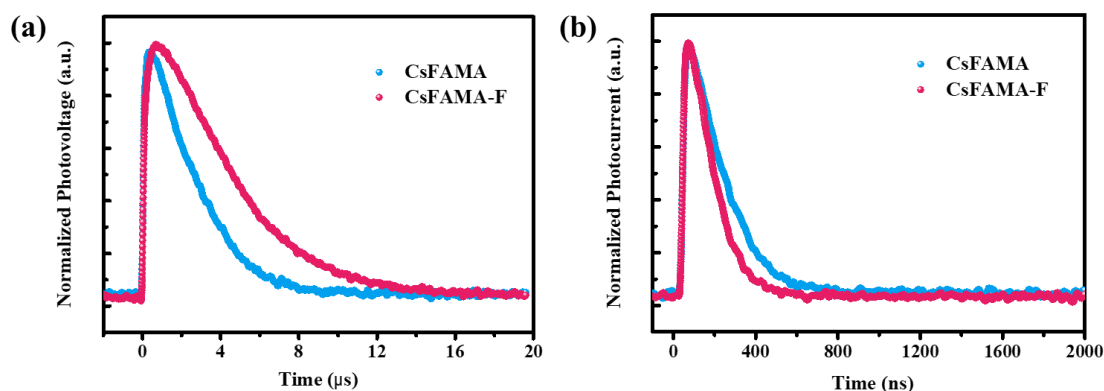
To quantitatively confirm the reduced density of defects, we fabricate perovskite devices by sandwiching the perovskite films between ITO and Au. We then characterize the evolution of the space-charge-limited current as a function of bias voltage (**Supplementary Figure 15**). At low bias voltage, the mobile carriers accounting for the current give a linear I–V curve, which is called the ohmic region. If the bias voltage increases, injected carriers start to fill the trap states, until the trap-filled limit (TFL) is reached at a voltage V_{TFL} . Within this bias voltage regime (below V_{TFL}), called the child region, the current is proportional to the square of the voltage ($I \propto V^2$)¹³. The defect density can be calculated according to the following equation¹⁴: $N_{defects} = \frac{2\varepsilon\varepsilon_0V_{TFL}}{eL^2}$, where ε is the relative permittivity of perovskite, ε_0 is the vacuum permittivity, L is the thickness of the perovskite film, and e is the elementary charge. We estimate the defect density ($N_{defects}$) to be $6.86 \times 10^{15} \text{ cm}^{-3}$ and $4.54 \times 10^{15} \text{ cm}^{-3}$ for the CsFAMA and CsFAMA-F devices, respectively. This result is in agreement with the values obtained from AS, indicating that the CsFAMA-F perovskite has fewer defects.



Supplementary Figure 15 The dark current–voltage characteristics of devices with ITO/perovskite/Au configuration.

Supplementary Note 12: TPC & TPV results and analyses

Fewer defects will lead to a reduced carrier recombination. To further confirm this, we perform transient photovoltage (TPV) and transient photocurrent (TPC) decay experiments to evaluate carrier dynamics in CsFAMA and CsFAMA-F PSCs. Shown in **Supplementary Figure 16**, the photovoltage decay time increases substantially from 3.31 μs in CsFAMA to 6.39 μs in CsFAMA-F, implying a lower charge carrier recombination rate. At the same time, the decay time of the photocurrent is reduced from 286 ns to 198 ns (**Supplementary Table 3**), which suggests an improved carrier transport in the CsFAMA-F device.



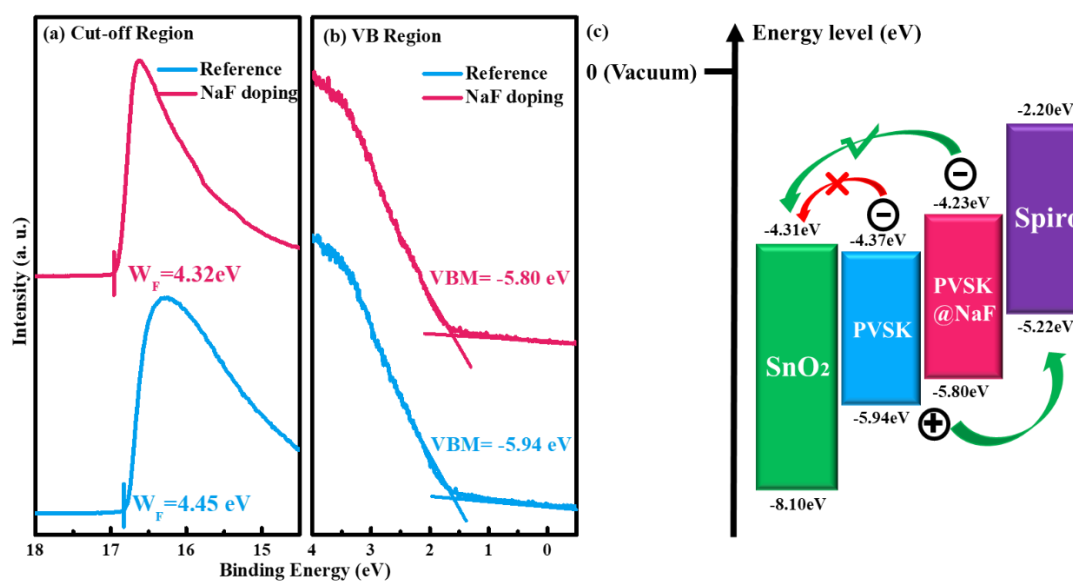
Supplementary Figure 16 The behavior of free carriers in perovskite solar cells without (CsFAMA) and with NaF additive (CsFAMA-F). (a) Transient photovoltage decay curves. (b) Transient photocurrent decay curves.

Supplementary Table 3. Photovoltage decay time ($\tau_{\text{recombination}}$) and photocurrent decay time ($\tau_{\text{transport}}$) of perovskite solar cells without (CsFAMA) and with NaF (CsFAMA-F).

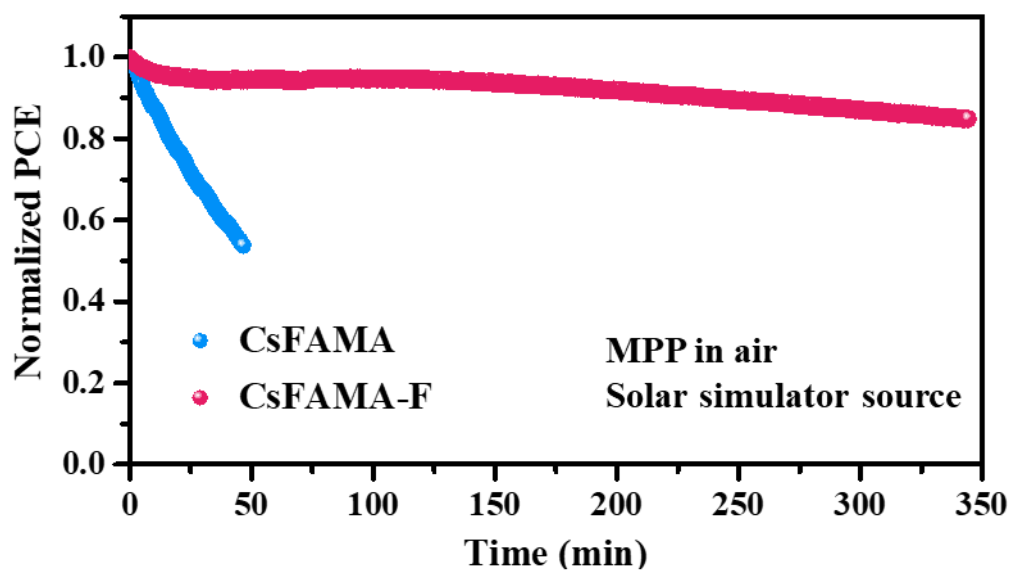
Sample	$\tau_{\text{recombination}}$	$\tau_{\text{transport}}$
CsFAMA	3.31 μs	286ns
CsFAMA-F	6.39 μs	198ns

Supplementary Note 13: UPS results and analyses

Supplementary Figure 17 shows the Fermi levels (E_F) and the valence band (VB) regions derived from ultraviolet photoelectron spectroscopy (UPS) spectra. The E_F of the CsFAMA and CsFAMA-F perovskites are -4.45 and -4.32 eV, respectively. The corresponding valence band maxima (VBM) are located at 1.49 and 1.48 eV below the E_F , respectively. In combination with the band gap acquired from the UV-visible spectra (**Fig. 1c**), one then obtains the energy levels of the CsFAMA and CsFAMA-F perovskite samples shown in **Supplementary Figure 17c**. The conduction band minimum (CBM) and VBM of CsFAMA perovskite are -4.37 eV and -5.94 eV, while those for the CsFAMA-F perovskite are -4.23 eV and -5.80 eV. The relative upshift of the CBM in the CsFAMA-F perovskite compared to CsFAMA, facilitates a more efficient electron injection from the perovskite into the ETL. This may also result in less charge accumulation at the interface between the absorber and the transport layer¹⁵ for the CsFAMA-F cell.



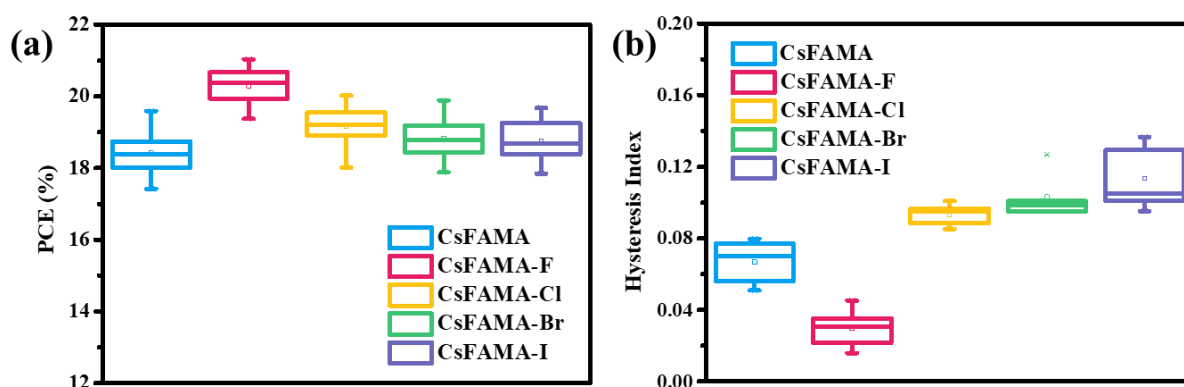
Supplementary Figure 17 Ultraviolet photoelectron spectroscopy (UPS) spectra of perovskite films. (a) Secondary electron cut-off region. (b) Valence band (VB) region. (c) Relative energy band diagram without (CsFAMA) and with NaF (CsFAMA-F).



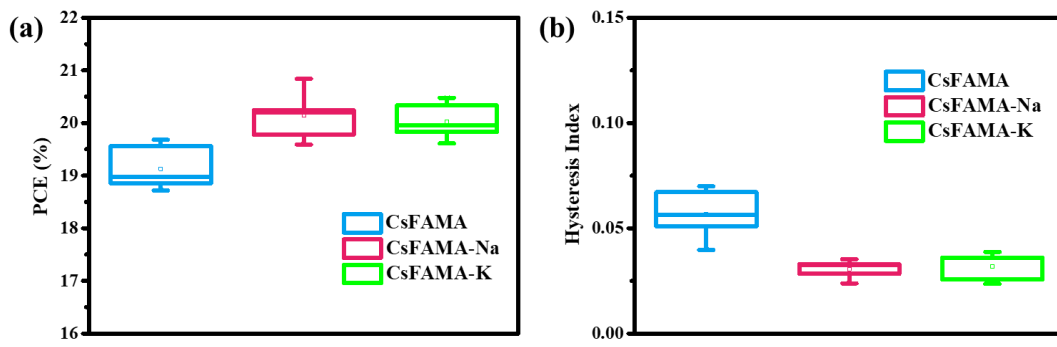
Supplementary Figure 18 MPP measurements in air. Evolution of normalized PCEs of unencapsulated devices under maximum power point (MPP) tracking and a continuous light irradiation with solar simulator source (100 mW/cm²) in air (with humidity about 20%, temperature about 50 °C).

Supplementary Note 14: NaX (X=F, Cl, Br, I) containing PSCs performance

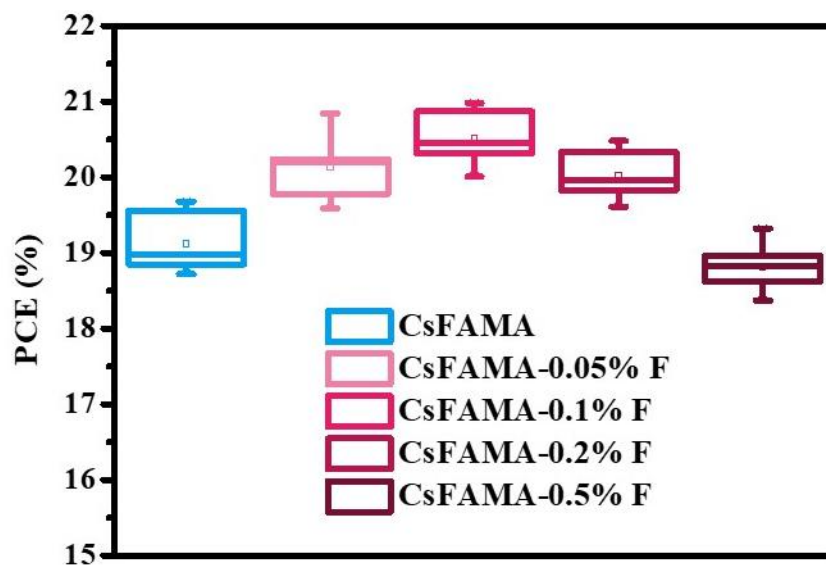
According to **Supplementary Figure 19b** we find that CsFAMA samples have a moderate J-V hysteresis. We speculate that this phenomenon can be linked to 1) more defects and more mobile ions such as iodide, MA (FA) in the reference sample and 2) Excess PbI₂ existed in the reference sample (**Supplementary Figure 3**) also lead to obvious hysteresis as previously reported¹⁶⁻¹⁷. Hysteresis can be diminished by the immobilization of mobile ions and vacancy defects such as iodide and MA (FA) via the incorporation of fluoride ions. Hysteresis is observed in other NaX (X=Cl, Br, I) containing PSCs, due to the mobile Na ions, as mentioned in the main text.



Supplementary Figure 19 The performance of reference (CsFAMA) and NaX (CsMAFA-X) containing perovskite solar cells. (a) PCE distribution. (b) Hysteresis index, defined as $HI = \frac{PCE(\text{Reverse}) - PCE(\text{Forward})}{PCE(\text{Reverse})}$



Supplementary Figure 20 The performance of the reference (CsFAMA) and NaF (CsFAMA-Na), KF (CsFAMA-K) containing perovskite solar cells. **(a) PCE distribution. (b) Hysteresis index HI.**



Supplementary Figure 21 The optimal content of NaF. The PCE distribution of the multi-PSCs based on reference (CsFAMA), NaF incorporation with different ratio (CsFAMA-0.05% F, CsFAMA-0.1% F, CsFAMA-0.2% F, CsFAMA-0.5% F).

Supplementary References

1. Roiland, C. et al. Multinuclear NMR as a tool for studying local order and dynamics in $\text{CH}_3\text{NH}_3\text{PbX}_3$ (X = Cl, Br, I) hybrid perovskites. *Phys. Chem. Chem. Phys.* **18**, 27133-27142 (2016).
2. Chen, Q. et al. The optoelectronic role of chlorine in $\text{CH}_3\text{NH}_3\text{PbI}_3(\text{Cl})$ -based perovskite solar cells. *Nat. Commun.* **6**, 7269 (2015).
3. Zheng, Y.C., Yang, S., Chen, X., Chen, Y., Hou, Y. & Yang, H.G. Thermal-induced Volmer–Weber growth behavior for planar heterojunction perovskites solar cells. *Chem. Mater.* **27**, 5116-5121 (2015).
4. Li, J.B., Chawla, V. & Clemens, B.M. Investigating the role of grain boundaries in CZTS and CZTSSe thin film solar cells with scanning probe microscopy. *Adv. Mater.* **24**, 720-723 (2012).
5. Thomas, A.M. & Nidia, G.L. Introducing DDEC6 atomic population analysis: part 1. Charge partitioning theory and methodology. *RSC Adv.* **6**, 47771–47801 (2016).
6. Thomas, A.M. Introducing DDEC6 atomic population analysis: part 3. Comprehensive method to compute bond orders. *RSC Adv.* **7**, 45552–45581 (2017).
7. Makhsud, I.S. et al. Suppression of atomic vacancies via incorporation of isovalent small ions to increase the stability of halide perovskite solar cells in ambient air. *Nat. Energy* **3**, 648-654 (2018).
8. Khelifi, S. et al. Investigation of defects by admittance spectroscopy measurements in poly (3-hexylthiophene):(6,6)-phenyl C61-butyric acid methyl ester organic solar cells degraded under air exposure. *J. Appl. Phys.* **110**, 094509 (2011).
9. Duan, H.-S., Yang, W., Bob, B., Hsu, C.-J., Lei, B. & Yang, Y. The role of sulfur in solution-processed $\text{Cu}_2\text{ZnSn}(\text{S},\text{Se})_4$ and its effect on defect properties. *Adv. Funct. Mater.* **23**, 1466-1471 (2012).
10. Ye, S. et al. A breakthrough efficiency of 19.9% obtained in inverted perovskite solar cells by using an efficient trap state passivator $\text{Cu}(\text{thiourea})\text{I}$. *J. Am. Chem. Soc.* **139**, 7504-7512 (2017).
11. Duan, H.-S. et al. The identification and characterization of defect states in hybrid organic-inorganic perovskite photovoltaics. *Phys. Chem. Chem. Phys.* **17**, 112-116 (2015).
12. Schottky, W. Vereinfachte und erweiterte Theorie der Randschicht-gleichrichter.

Zeitschrift für Physik **118**, 539-592 (1942).

13. Huang, Y. et al. The intrinsic properties of $\text{FA}_{(1-x)}\text{MA}_x\text{PbI}_3$ perovskite single crystals. *J. Mater. Chem. A* **5**, 8537-8544 (2017).
14. Liu, Z. et al. Chemical reduction of intrinsic defects in thicker heterojunction planar perovskite solar cells. *Adv. Mater.* **29**, 1606774 (2017).
15. Kim, H.-S. et al. Mechanism of carrier accumulation in perovskite thin-absorber solar cells. *Nat. Commun.* **4**, 2242 (2013).
16. Hui, Y. et al. Native defect-induced hysteresis behavior in organolead iodide perovskite solar cells. *Adv. Funct. Mater.* **26**, 1411-1419 (2016).
17. Jiang, Q. et al. Planar - Structure Perovskite Solar Cells with Efficiency beyond 21%. *Adv. Mater.* **29**, 1703852 (2017)